NANO LETTERS

Letter

pubs.acs.org/NanoLett

Mapping Bright and Dark Modes in Gold Nanoparticle Chains using Electron Energy Loss Spectroscopy.

Steven J. Barrow,[†] David Rossouw,[‡] Alison M. Funston,*[,§] Gianluigi A. Botton,*[,‡] and Paul Mulvaney*[,†]

[†]School of Chemistry and Bio21 Institute, University of Melbourne, Parkville, Victoria 3010, Australia

[‡]Department of Materials Science and Engineering, McMaster University, Hamilton, Ontario Canada

[§]Chemistry Department, Monash University, Clayton, Victoria 3800, Australia

Supporting Information

ABSTRACT: We present a scanning transmission electron microscopy−electron energy loss spectroscopy (STEM-EELS) investigation of gold nanosphere chains with lengths varying from 1 to 5 particles. We show localized EELS signals from the chains and identify energy-loss peaks arising due to l = 1, 2, 3, 4, and 5 plasmon modes through the use of EELS mapping. We also show the evolution of the energy of these modes as the length of a given chain increases, and we find that a chain containing N particles can accommodate at least N experimentally observable modes, in addition to the transverse mode. As the chain length is increased by the addition of one more gold particle to the chain, the new N + 1 mode becomes the highest energy mode, while the existing modes lower their energy and eventually asymptote as they delocalize along the chain. We also show that modes become increasingly difficult to detect with the EELS technique as l approaches N. The data are compared to numerical simulations.

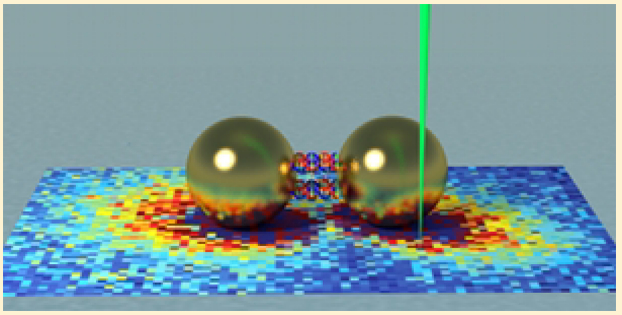

KEYWORDS: *STEM-EELS, dark modes, Surface Plasmon, Electron-Energy Loss Spectroscopy, Nanoparticle Chains*

One-dimensional gold nanoparticle chains ("plasmonic polymers"[1]) provide an interesting system for controlling interactions of light with matter. In such chains, light is not absorbed by a single particle but excites collective plasmon modes that can exist over the entire structure. The optical properties of the chain are governed by the radius of the spheres, R, the number of particles in the chain, N, and the interparticle spacing, d. The coupling between the spheres is a strong function of the ratio d/R. For chemically assembled chains, the spacing maybe as little as 1 nm, leading to strong coupling of the optically driven near-fields.[2] As a result, various potential applications of these tunable plasmonic systems have been mooted, including surface enhanced raman spectroscopy (SERS),[3−7] solar light harvesting and photocatalysis,[8,9] chemical and biological sensing,[10−15] optical circuitry[16,17] and metamaterials.[18−21]

Thus, far, most studies of nanoparticle chains have been optical studies. These have revealed that the dipolar plasmon resonance of a single particle splits into at least two resonances upon coupling to another particle, forming a dimer structure.[2,17,22−27] This interaction can be understood in terms of plasmon hybridization theory. A longitudinal plasmon mode is excited when the electric field of the incoming light plane-wave is polarized parallel to the interparticle axis giving rise to an attractive (or "bonding") interaction. Conversely, the transverse mode is excited when the electric field of the incoming light plane-wave is polarized perpendicular to the interparticle axis resulting in a repulsive (or "antibonding") interaction. Thus, the energy of the coupled longitudinal resonance is red shifted compared to the plasmon resonance energy of a single sphere, while the energy of the transverse mode is blue shifted. In addition to these modes, coupled plasmon resonances are also predicted that have no net dipole (termed "dark" modes), and hence cannot couple to plane-wave incident light.

Elongation of the nanoparticle assembly to a chain enables further plasmon hybridization across the structure, and higher energy modes delocalized along the chain become more important. Initially, we will discuss the possible longitudinal modes. For these, the modes may be labeled according to their mode number (l = 1, 2, 3...N) from lowest to highest energy. Conceptually, these modes may be considered as the finite nanoparticle array form of Fabry−Perot-like resonances, or, alternatively, as the dipole, quadrupole, octupole, and so forth, modes of localized surface plasmon resonances in single nanoparticles. The lowest energy l = 1 mode is the fundamental dipole mode. It couples most strongly to the incident light field as the individual dipoles of each nanoparticle are aligned resulting in a large dipole moment for the coupled resonance (see Figure S1 of the Supporting Information for a schematic of the dipole alignment of this mode). This is often termed the

Received: March 10, 2014
Revised: June 8, 2014
Published: June 23, 2014

   dx.doi.org/10.1021/nl5009053 | *Nano Lett.* 2014, 14, 3799−3808

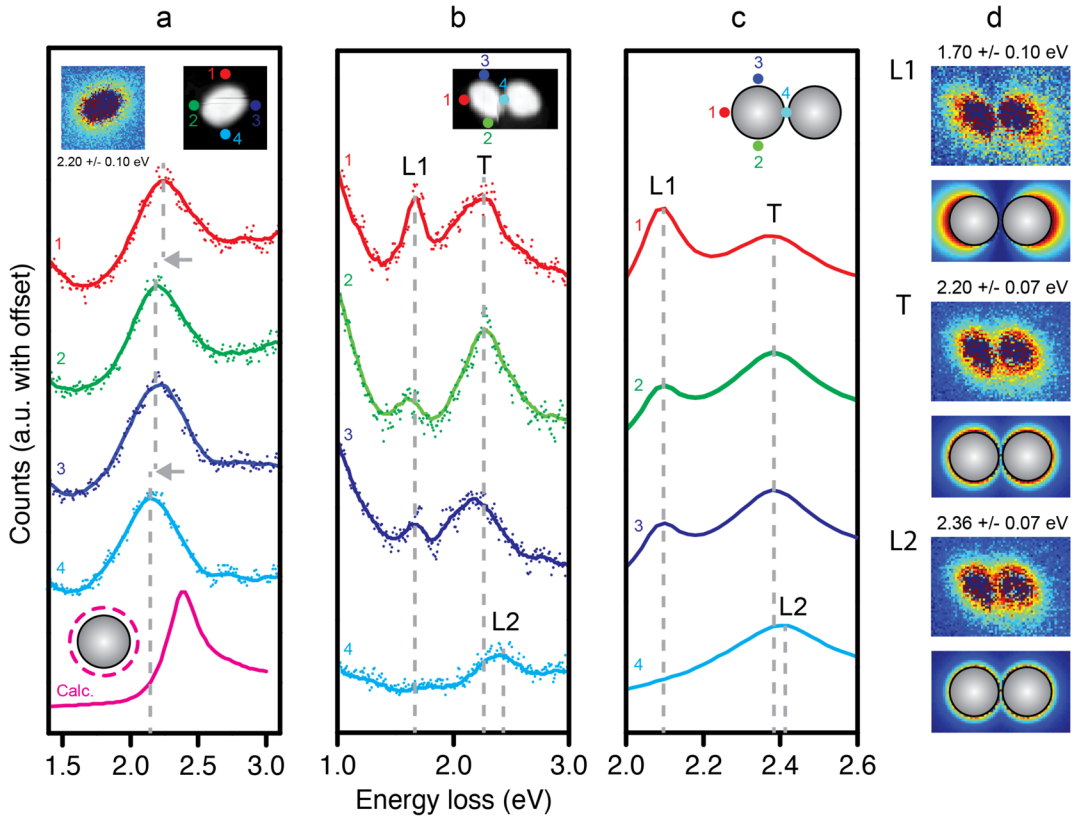

Figure 1. (a) EELS spectra of a single nanoparticle taken at the locations indicated by the numbers in the dark-field image of the sphere in the upper right inset. The bottom (pink line) spectrum is a summed EELS spectrum of a 45 nm diameter gold nanopshere (as indicated in the bottom left inset) calculated via BEM. (Upper left inset) Experimental EELS map of the sphere. Experimental (b) and modeled (c) EELS spectra of a nanoparticle dimer taken at the locations indicated by the numbers in the insets. Inset of (b) shows a dark-field image of the dimer. (d) Experimental (upper) and modeled (lower) EELS maps of the (L1) $l = 1$, (T) transverse, and (L2) $l = 2$ modes present within the dimer. Gold nanospheres used in this work have diameters of 45 nm.

longitudinal mode and has also been referred to as the super-radiant mode.[28] The higher energy modes, $l = 2, 3, 4...N$ do not couple as strongly (or at all), depending upon the mode number, to an incoming electromagnetic field and have been referred to previously as subradiant modes. Modes with even l are dark modes (and so have previously been referred to as "dark subradiant modes"), possessing no net dipole moment at all and therefore are unable to be excited by plane-polarized light. Those with odd l do have a net dipole moment, albeit smaller than the super-radiant, and are able to couple weakly to plane-wave incident radiation; these have been called "bright subradiant modes" (Figure S1 of the Supporting Information shows schematics of the charge distributions of these bright and dark modes). Here, we use the designations $l = 1, 2, 3...N$ to differentiate between these possible modes rather than the subradiant terminology. In addition to these longitudinal modes, transverse modes are also possible. Dark-field microscopy (DFM) can be used to collect the spectra of the optically active modes via their far-field scattering but normally only the super-radiant and transverse modes are readily discernible. An alternative approach is to use electron energy loss spectroscopy (EELS) to study the coupling of fast (80–300 keV) electrons to the plasmon modes of the system.

EELS has long been used to probe the plasmon modes of metal nanoparticles and metal films. The theory was developed by Fujimoto in 1967[29,30] and experiments to distinguish between bulk volume plasmons, surface plasmons on flat metal films, and localized surface plasmon modes in metal nanoparticles have been previously reported.[31] However, the advent of atomic-resolution imaging through scanning transmission electron microscopy (STEM) coupled with the improved energy resolution of EELS detectors now enables the interrogating electron beam to map the energy loss with unprecedented spatial and energy resolution.[32,33] Furthermore, the combination of STEM with EELS allows simultaneous morphological and spectral analysis of individual nanostructures. Single metal nanoparticles including spheres,[32,34,35] rods,[32,36] and nanowires[37−39] as well as nanosphere and nanorod dimers[36,40,41] have been analyzed using STEM-EELS. This approach provides an enormous advantage over the current cumbersome and time-consuming methods used to correlate the optical scattering spectra with EM images.[42−47]

The exact relationship between the energy-loss map for a given plasmon resonance and the optical near-field map remains the subject of intense discussion. It has been predicted that the energy-loss map is directly related to the local density of states for single nanoparticles.[48] In contrast, studies on coupled systems that incorporate theoretical simulations along with experimental results suggest that the energy-loss map is representative of the electric field strength.[49−52] Energy-loss maps of the super-radiant mode in nanosphere dimers display the highest loss probability at the ends of the nanoparticles, furthest from the gaps.[53,54] This result is also obvious for larger aggregates.[32,51] In contrast, the near-field enhancement associated with this mode is calculated to be greatest in the interparticle gap, which is in agreement with optical experi-

dx.doi.org/10.1021/nl5009053 | Nano Lett. 2014, 14, 3799−3808

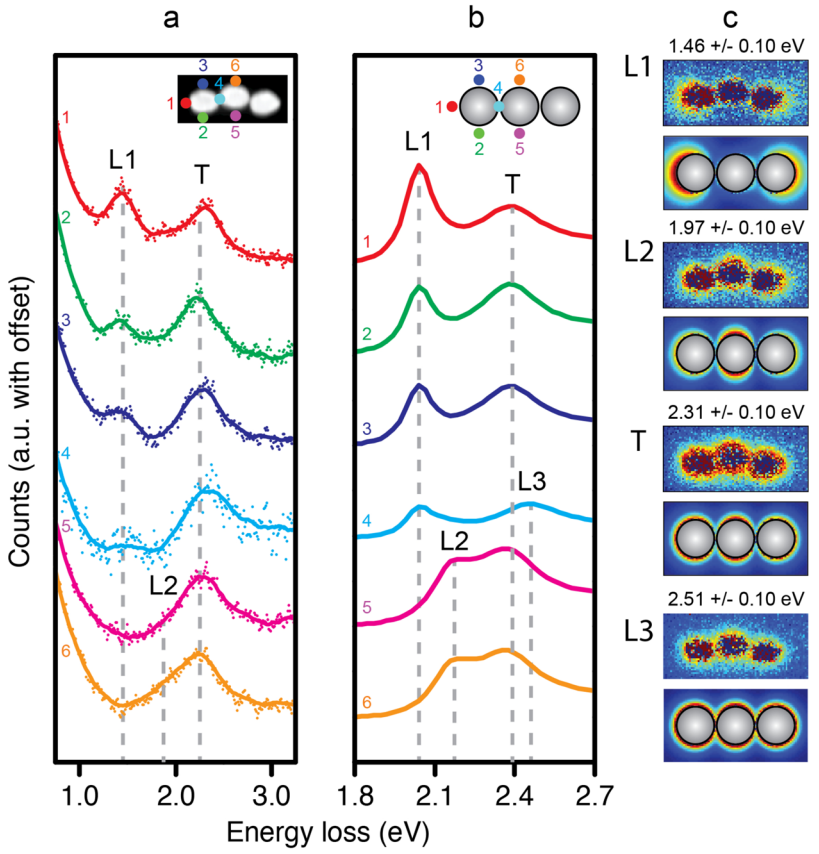

Figure 2. Experimental (a) and modeled (b) EELS spectra of the three particle chain taken at the locations indicated by the numbers in the insets. Inset of (a) shows a dark-field image of the structure. (c) Experimental (upper) and modeled (lower) EELS maps of the (L1) $l = 1$, (L2) $l = 2$, (T) transverse and (L3) $l = 3$ modes present within the three particle chain. Gold nanospheres used in this work have diameters of 45 nm.

ments.[55−57] While energy loss spectra of the dark modes of silver nanoparticle dimers have been reported,[40,58,59] few EELS maps of this mode have been published.[58] The EELS map of the analogous dark mode in dimers of gold nanorods, roughly end-to-end aligned, has been reported,[54] although the slightly asymmetric alignment of the nanorod dimer investigated, which can result in dark modes becoming optically bright,[26] potentially impacts the map and mode energy.[54]

In this study, we extend previous STEM-EELS measurements by analyzing one-dimensional chains of gold nanospheres. We observe the energy-loss peaks for super-radiant modes and transverse modes, as well as bright and dark subradiant modes within the nanosphere chains and confirm the presence of these modes with EELS mapping and numerical calculations. We then highlight the evolution of these modes as their energies change with increasing chain length. Subradiant modes are particularly important for future waveguiding applications as they may provide a lower loss mechanism for energy guiding.[28] The results obtained are compared to previous dark-field measurements of bright modes.[2]

Results. Figure 1a shows the EELS spectra for a single gold nanosphere with a diameter of 45 nm. The spectra are numbered according to the positions where they were collected as shown in the dark-field image in the upper right inset. In agreement with previous reports,[60,61] for electron excitation around the edge of the particle a single energy-loss peak is observed at 2.1 eV. This energy-loss corresponds to excitation of the dipolar mode, confirmed by the EELS map (upper left inset of Figure 1a). Although the energy of the sphere's surface plasmon is expected to be fixed around the nanoparticle, our EELS measurements record a slight redshift (a difference of 0.11 eV is shown from spectra 1 to 4 in Figure 1a) of the surface plasmon from top to bottom (Figure 1a). We attribute the redshift to a slight accumulation of carbonaceous material around the nanoparticle formed during the beam scan.[40] The presence of additional carbon is observed in TEM images (see Figure S2 of the Supporting Information) acquired after the scan, which acts to modify the local dielectric environment of the particle, causing a shift of the surface plasmon resonance energy. The observed redshift demonstrates the sensitivity of the EELS technique to small changes in the local environment, and while the carbon materials likely damps the surface plasmon and is thus undesirable, it does not interfere with our interpretation of the signal origin. It should also be noted that the sphere appears ellipsoidal in the upper right inset, even though the bright-field image (see Figure S2 of the Supporting Information) shows that the particle is indeed spherical. This artifact is due to a small distortion in the electron probe scanning system (the scanned area can be seen in the background contrast of Supporting Information Figure S2). The upper left inset of Figure 1a shows an EELS scattering intensity map of the 2.1 eV dipole mode of the single particle. The energy-loss is evident around the entire circumference of the sphere, as to be expected. All experimental EELS maps in the present work have been normalized to the intensity of the zero-loss peak, as outlined in the Supporting Information. It should be pointed out that although the trends in the modeled data for the single sphere and the other structures presented in

dx.doi.org/10.1021/nl5009053 | *Nano Lett.* 2014, 14, 3799−3808

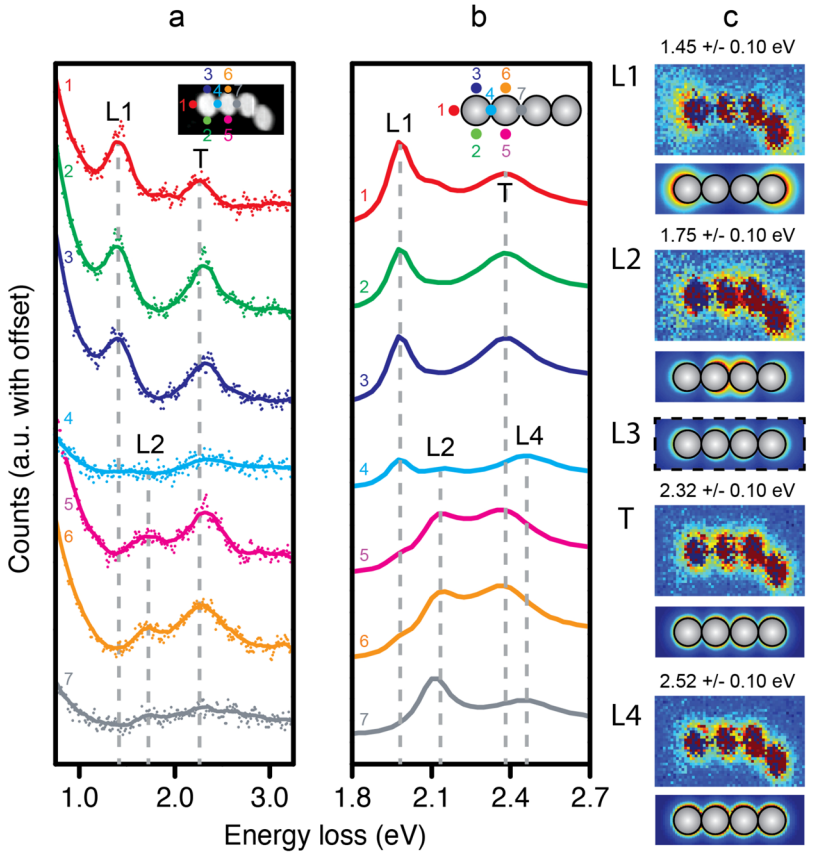

Figure 3. Experimental (a) and modeled (b) EELS spectra of the four particle chain taken at the locations indicated by the numbers in the insets. Inset of (a) shows a dark-field image of the structure. (c) Experimental (upper) and modeled (lower) EELS maps of the (L1) $l = 1$, (L2) $l = 2$, (T) transverse (L3) $l = 3$ (model only, calculated using the Drude model), and (L4) $l = 4$ modes present within the four particle chain. Gold nanospheres used in this work have diameters of 45 nm.

this work match the experimental data, the absolute energies of the EELS peaks do not, as is apparent from Figure 1a. Energy differences of this order of magnitude between experimentally observed and calculated data have previously been accounted for by inclusion of a thin dielectric shell, which in our system is most likely due to DNA.[40] Inclusion of a substrate or modification of a homogeneous dielectric constant have also previously been used to obtain better absolute agreement. Here, we focus on the trends in the experimental data with the view of mode assignment in reference to the modeled data rather than obtaining exact energy agreement between the two. As such, we use a homogeneous dielectric environment (no substrate) with $n = 1.33$ for all modeling.

Figure 1b shows the EELS spectra of a gold nanoparticle dimer with modeled spectra shown in Figure 1c calculated using BEM numerical methods.[52] Consistent with optical and EELS studies of similar systems,[2,40,62] plasmon coupling within the dimer splits the electron energy loss into two peaks, one at 2.3 eV and the other at 1.7 eV. The energy-loss peak at 1.7 eV has highest relative intensity for excitation at the tips of the dimer (position 1 in the insets), with the intensity of the 2.3 eV peak being relatively constant in the immediate vicinity of the particle boundaries. These resonances are in agreement with literature as the excitation of the $l = 1$ (super-radiant) and transverse modes respectively from both peak energy,[2] electron beam excitation position,[40,58] and EELS maps.[58] The EELS map for the $l = 1$ mode (labeled as L1 in Figure 1d) shows a high loss probability at the opposite tips of the dimer with no intensity located in the interparticle gap. A third electron energy loss peak is observed at 2.4 eV when the electron beam is focused in the interparticle gap (position 4 in the insets of Figure 1b,c). This is assigned to the $l = 2$ dark subradiant mode. The experimental and modeled EELS maps for both the transverse and $l = 2$ modes (labeled as T and L2 in Figure 1d) of the dimer are similar,[54,58] showing even scattering intensity around the perimeter of the dimer, except in the region of the interparticle gap. For the dimer the $l = 2$ mode shows a slightly higher loss probability in the interparticle gap compared to the transverse mode, relative to the loss probability around the edges of the structure. However, even though this trend is in agreement with the calculations shown, the calculations predict the difference between the modes to be smaller than the precision of our measurements. Therefore, we cannot spatially distinguish between the two modes definitively. This is highlighted in Figure S3 of the Supporting Information, where line profiles of the experimental and calculated EELS maps for the $l = 1$, 2 and transverse modes for the dimer are shown.

In Figure 2, we show experimental and calculated EELS spectra for a gold nanoparticle trimer. In Figure 2a, experimental spectra are shown collected at the six positions marked in the inset image. There are two clear resonances at 2.3 and 1.45 eV that are excited at positions 1, 2, and 3. The 1.45 eV peak is strongest for excitation at the end of the trimer and this supports assignment as the $l = 1$ (super-radiant) mode for this structure. This is further shown by the EELS map for

dx.doi.org/10.1021/nl5009053 | Nano Lett. 2014, 14, 3799−3808

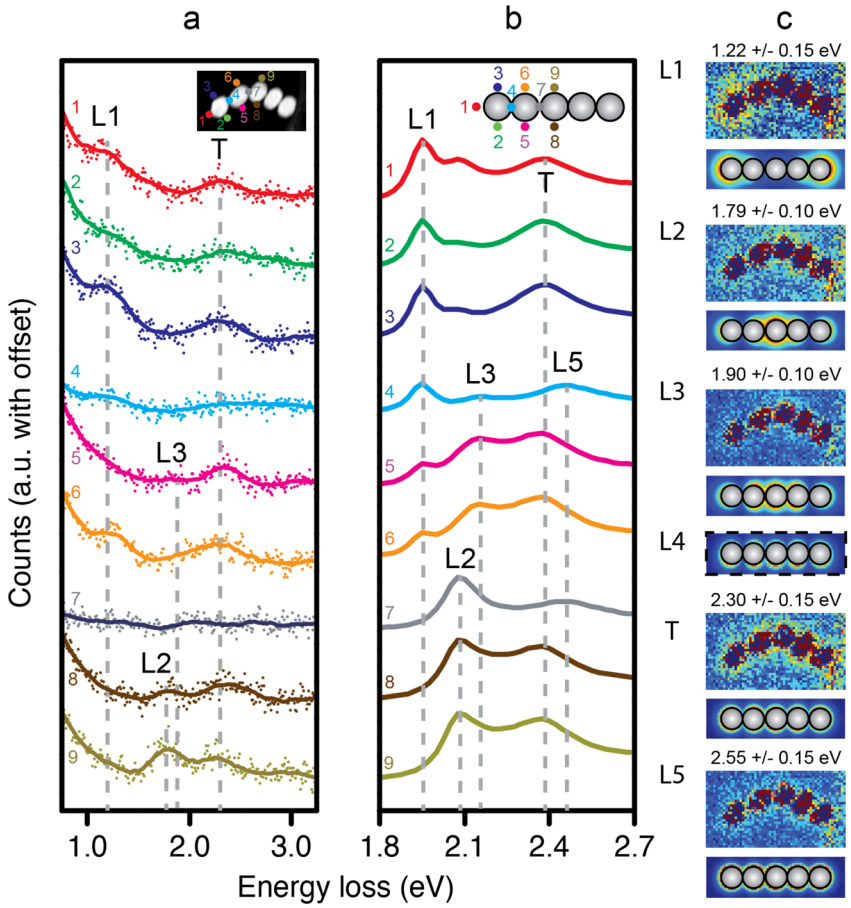

Figure 4. Experimental (a) and modeled (b) EELS spectra of the five particle chain taken at the locations indicated by the numbers in the insets. Inset of (a) shows a dark-field image of the structure. (c) Experimental (upper) and modeled (lower) EELS maps of the (L1)l = 1, (L2) l = 2, (L3) l = 3, (T) transverse (L4) l = 4 (model only, calculated using the Drude model), and (L5) l = 5 modes present within the five particle chain. Gold nanospheres used in this work have diameters of 45 nm.

this peak, labeled as L1 in Figure 2c, which reveals high energy-loss intensity around the ends of the nanoparticle chain. In Figure 2a, we can see that the 2.3 eV peak is relatively intense for excitation around the end particle and either side of the central particle, characteristic of a transverse mode. The EELS map for this mode (labeled T in Figure 2c) along with the energy of the loss peak supports designation as the transverse mode as the scattering intensity is uniform around the entire perimeter of the trimer.

In Figure 2b, we present modeled EELS spectra for the trimer, which reproduce the relative intensities of the modes and mode energies very well. The modeled spectra at positions on either side of the central particle (positions 5 and 6 in Figure 2b) show an energy-loss peak that lies at 2.16 eV, which is in-between the super-radiant and transverse mode energies. While this peak is not obvious in the experimental data, there is a degree of asymmetry in the loss-peak attributed to the transverse mode (at a similar energy). Multipeak fitting of the asymmetric transverse peak reveals a low intensity peak at 2 eV that overlaps with the transverse mode (see Supporting Information Figure S4 for an image of the fit). An EELS map of this peak with a modeled EELS map of the 2.16 eV peak can be seen in Figure 2c, labeled as L2. The modeled map shows increased scattering intensity around the central nanoparticle, which is indicative of the l = 2 (dark subradiant) mode for the trimer. However, the increased intensity is not as clear in the experimental map.

The modeling in Figure 2b shows that the highest energy mode for this structure is produced upon excitation in the interparticle gap (position 4) and corresponds to the excitation of the l = 3 (bright subradiant) mode. This shift is just resolved in the experimental spectrum at this point. The modeled and experimental EELS maps at this energy, labeled as L3 in Figure 2c, reveal energy-loss probability around the entire perimeter of the structure for this mode.

In Figure 3a, we present experimental spectra for a four particle chain and it can be seen that it shows similar behavior to the three particle chain presented previously. Excitation at the end of the chain (positions 1, 2, and 3) gives rise to energy-loss peaks at 1.4 and 2.3 eV. The intensity of these peaks remains relatively constant at excitation positions around the end particle. EELS maps for the 1.4 eV peak can be seen in Figure 3c with the label L1, which shows greatest energy-loss probability at either end of the nanoparticle chain, and is therefore attributed to the l = 1 (super radiant) mode for this structure. EELS maps for the 2.3 eV peak, labeled as T in Figure 3c, show that energy-loss occurs evenly around the nanoparticle chain at this energy.

Excitation on either side of the second nanoparticle (positions 5 and 6) reveals two energy-loss peaks at 1.7 and 2.3 eV. As discussed above, the latter peak is due to the

dx.doi.org/10.1021/nl5009053 | *Nano Lett.* 2014, 14, 3799−3808

transverse mode, and EELS maps for the former can be seen in Figure 3c in the image labeled L2. This mode is designated as the $l = 2$ (dark subradiant) mode, as the EELS maps show increased energy-loss probability around the central two particles of the four particle chain, which is in agreement with the EELS map of the $l = 2$ mode in the trimer, where increased loss probability was present around the central particle.

It should be noted that the $l = 3$ mode for the four particle chain has not been detected in the experimental data or modeled spectra but would be expected to give an EELS peak at an energy that lies in between that of the $l = 2$ and transverse modes.[28] It is possible that the EELS peak for this mode is masked by that of the transverse mode due to the width and proximity of the peaks in much the same manner as the $l = 2$ mode of the three particle chain. In order to model the EELS map for this mode (labeled as L3 in Figure 3c), the Drude model dielectric function for gold was used, whereby the shielding effect of high order modes and interband transitions was removed. It can be seen that this mode shows a very similar EELS map compared to the transverse mode, meaning that the spatial selectivity of the EELS technique is unable to clearly distinguish between the $l = 3$ and transverse modes. We suggest that this, combined with poor coupling to the incident electron beam, results in the $l = 3$ mode being masked by the transverse and high order modes, making experimental detection difficult.

Excitation at position 4 in Figure 3a reveals a very weak and broad peak at approximately 2.3 eV. The weak intensity of this peak is most likely due to excess ligand present in the interparticle gap, as it can be seen that there is a reduction in the overall signal acquired. Similarly, excitation at position 7 shows a decrease in acquired signal. The modeled EELS spectra in Figure 3b at these positions predict the highest energy peak for this structure, which is only present in the spectra collected at these positions. This is consistent with the excitation of the $l = 4$ (dark subradiant) mode, and the experimental and modeled EELS maps of this mode can be seen in the image labeled at L4 in Figure 3c. The modeled EELS map shows even scattering around the perimeter of the structure.

In Figure 4, we present the spectra for a five particle chain. Figure 4a highlights the experimental data, however, we will begin with a discussion of the modeled data in Figure 4b. Excitation around the end particle (positions 1, 2, and 3) gives rise to two peaks with energies at 1.9 and 2.4 eV in the modeled data. EELS maps for the 1.9 eV peak can be seen in Figure 4c, labeled as L1. The modeled map of this peak clearly shows maximum energy-loss occurring at either end of the nanoparticle chain, displaying characteristic $l = 1$ (super radiant) mode scattering behavior. Figure 4c shows EELS maps for the 2.3 eV peak (labeled T) and shows evidence of a transverse mode as scattering is evident evenly around the nanoparticle chain, except in the region of the interparticle gaps.

EELS excitation at either side of the central, third particle (positions 8 and 9) in the five particle chain in Figure 4b gives rise to a transverse peak at 2.4 eV and another peak at 2.1 eV. EELS maps for the 2.1 eV mode can be seen in Figure 4c, labeled as L2. The modeled map shows increased scattering intensity around the central nanoparticle in the five particle chain. This is consistent with the trimer and four particle chain and can be attributed to the $l = 2$ (dark subradiant) mode.

Excitation either side of the second particle in the chain (positions 5 and 6) in the modeled data shows three peaks: one at 2.4 eV (the transverse mode), another at 2.15 eV, and a third at 1.9 eV ($l = 1$ mode). The EELS map for 2.15 eV peak can be seen in Figure 4c L3 and shows scattering intensity around the central three particles in the chain but of weaker intensity than the $l = 2$ (dark subradiant) mode in Figure 4c, labeled L2. This mode is presumably the $l = 3$ mode, due to the peak energy.

Positions 4 and 7 both involve EELS excitation at the interparticle gaps in the five particle chain. Modeling of the spectra at these positions shows the highest energy peak for this structure and the presence of either 1 (position 7) or 2 (position 4) lower energy modes. The higher energy mode arises from the excitation of the $l = 5$ (bright subradiant) mode, the experimental and modeled EELS maps for which can be seen in Figure 4c, labeled as L5. The modeled EELS map of this mode shows scattering around the perimeter of the structure as well as in the interparticle gaps. In addition to the $l = 5$ mode, the spectrum for excitation at position 4 also shows evidence of the $l = 1$ and 3 modes with peaks at 1.9 and 2.15 eV present with position 7 only exhibiting the $l = 2$ mode at 2.1 eV.

The experimental data in Figure 4a are generally consistent with the trends of the modeled data, despite the low signal-to-noise ratio. Excitation at positions 1, 2, and 3 agree with the modeled data with the $l = 1$ and transverse mode evident at 1.15 and 2.3 eV, respectively. The experimental energy loss map at 1.15 eV (Figure 4c L1) indicates a high probability of loss around the left-most nanoparticle only, whereas the modeled map shows a high probability loss around both ends of the structure. The bright-field TEM of this structure shows the presence of a thick region in the carbon support film concentrated around the right-most particle. This results in a poorer signal collected from this region and a reduction of intensity in the experimental map. Excitation at positions 8 and 9 also agree with the modeled data within the signal-to-noise ratio observed. However, no readily discernible peaks are observed in the experimental spectra for excitation in the interparticle regions of the five particle chain. The tails of the zero-loss peak at these positions (4 and 7 in Figure 4a) are also essentially absent, indicating that most likely the gaps are too small or there is too much ligand at these positions for the electrons to penetrate. Although both the experimental spectra at positions 5 and 6 show the transverse mode at 2.3 eV, the spectrum collected at position 6 only shows evidence of the super-radiant mode at 1.2 eV, while the spectrum collected at position 5 shows evidence of a peak at 1.87 eV, which is likely to correspond to the $l = 3$ mode (2.15 eV peak in modeled data).

Similar to the $l = 3$ mode in the four particle chain, the $l = 4$ mode of the five particle chain has also not been detected in the experimental or modeled data. The modeled EELS map for this mode (also calculated using the Drude model for gold) is shown in image L4 in Figure 4c. The map for this mode is very similar to the map of the transverse mode for this structure, therefore, similar conclusions can be drawn compared to the $l = 3$ mode of the four particle chain. The excitation of the $l = 4$ mode of the five particle chain is likely masked by the excitation of the transverse and higher order modes, due to poor coupling to the incident beam, as well as significant overlap of the EELS maps for it and the transverse mode, meaning that both modes are potentially excited at the same time.

Discussion. The evolution of subradiant plasmon modes of the higher-order oligomers is critical for an understanding of the transformation of structurally localized plasmon modes within the oligomer to delocalized waveguiding modes in a nanoparticle "polymer". The high energy $l = 2$ mode within the

dx.doi.org/10.1021/nl5009053 | Nano Lett. 2014, 14, 3799−3808

dimer identified above can be considered to be the first dark subradiant mode for a plasmonic oligomer with $N = 2$. The dipoles of the particles are aligned along the interparticle axis with opposing oscillation (see Figure S1 of the Supporting Information) leading to a highly repulsive interaction (analogous to an antibonding hybridization within MO theory), hence the relatively high energy of the observed resonance. As the number of nanoparticles in the chain is increased, both dark and bright subradiant modes with different spatial localization become possible. This trend is apparent from the position-dependent EELS spectra and maps of higher-order oligomers. The longest oligomer investigated ($N = 5$) displays the most complex EELS response with multiple bright and dark subradiant ($l = 2$, 3, 4, and 5) modes observed.

For all of the $N = 2$, 3, 4, and 5 oligomers, the lowest electron energy loss peak is predominantly excited when the electron beam is positioned at the tip of the nanoparticle chain (position 1 in Figures 3, 4, and 5). The EELS maps at the energies of the loss peak for this mode (images labeled as L1 in Figures 2c, 3c, and 4c for the 3, 4, and 5 particle chains, respectively) show the highest loss probability at either tip of the nanoparticle chain (except for the right-most end of the five particle chain, which was next to the carbon support on the TEM grid and resulted in reduced signal intensity), analogous to the loss probability for the longitudinal bonding interaction within the dimer. Thus, this mode for all oligomers is identified as the super-radiant $l = 1$ mode. The evolution of the loss energy of this peak is plotted as a function of chain length in Figure 5. As the number of nanoparticles in the chain is increased, this loss peak shifts to lower energy indicative of delocalization throughout the length of the chain. While it is not reached in the data shown here, the energy of the mode decreases as the number of nanoparticles increases and appears to be reaching a plateau. As it is a bright mode it is able to be excited optically, and the trend in energy as a function of nanoparticle number agrees with that observed for optical experiments on these nanoparticle chains.[2] Including the resonances from a single sphere and the super-radiant mode of the dimer, the peak shift is of the order of 1 eV from $N = 1$ (2.1 eV) to $N = 5$ (1.2 eV), characteristic of the very strong near-field coupling in these assembled nanoparticle chains with small interparticle spacings.[2] Its has also been shown that small disorders in linear chains of nanoparticles has little effect on the energy of the super-radiant mode.[2,63,64] The EELS responses observed for all modes and chains display no signature of localized plasmonic responses within the chain length that are expected in structures where the disorder has a significant impact on the plasmonic response.[64]

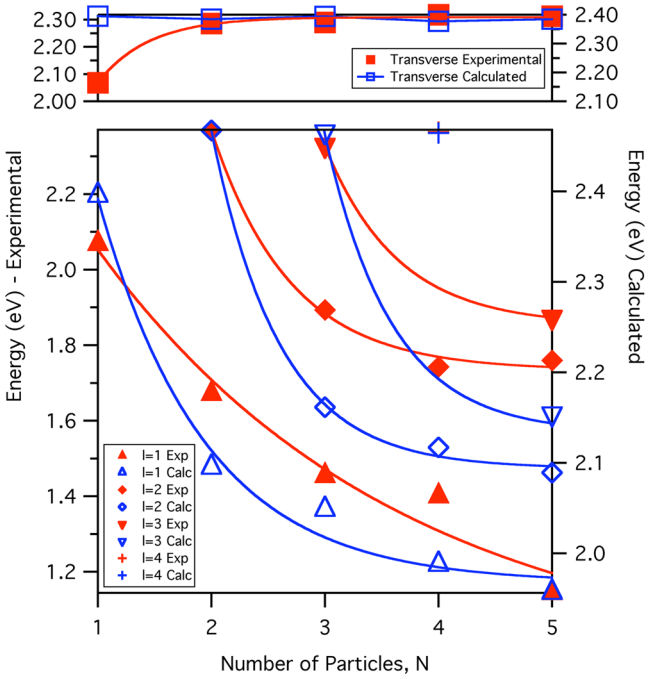

Figure 5. A plot of experimental (E, red lines) and calculated (C, blue lines) mode evolution versus chain length with longitudinal $l = 1$ (red closed triangle), $l = 2$ (red closed diamond), $l = 3$ (blue open triangle), $l = 4$ (plus symbol), and transverse (red closed square) modes shown. Lines are fits to the data with exponential curves being imposed on the data in some cases.

It is important to note that any discussion that focuses on a limited number of resonances within nanochain structures is incomplete, as theoretically the number of plasmon modes that a structure can accommodate is infinite.[65,66] We have considered here, however, the highest energy subradiant mode observable to be the mode in which the dipoles of each individual particle in the chain are directly aligned along the interparticle axis with opposite sense of oscillation (that is a node in between each particle with every interparticle interaction being highly repulsive). This allows for the same number of modes as particles in the chain for each structure (for example, for $N = 2$, two radiant modes, $l = 1$ and $l = 2$; for $N = 5$, five possible modes, $l = 1$, $l = 2$, $l = 3$, $l = 4$, and $l = 5$). See Figure S1 of the Supporting Information for wave diagrams of these modes. While this is a somewhat arbitrary limit, it is reasonable given the EELS modes identified for the dimer in which only two radiant modes, $l = 1$ and $l = 2$, are observed in both this and previous studies of the EELS response of dimers.[36,40,41] Additionally, our experimental results are explained very well upon consideration of only these modes with no further experimentally observed or modeled modes apparent. However, despite this it is known that for longer chains the energy of the modes converge and therefore we cannot rule out some contribution to the highest energy loss-peak observed from higher order modes.

The mode number for the radiant modes may then be categorized according to their order. Thus, $l = 1$ corresponds to the lowest energy collective dipole antenna harmonic, the bright super-radiant mode, which has a fundamental wavelength proportional to twice the length of the chain. The next lowest energy mode for all oligomers is the dark subradiant ($l = 2$) mode with a central node and no net transition dipole. This is the "antibonding" mode identified for the dimer and is also observed for the higher order oligomers (at 2, 1.8, and 1.7 eV for $N = 3$, 4, and 5, respectively). The energy of the $l = 2$ mode originates at an energy that is higher than the transverse mode in the dimer (2.4 eV) but then lowers in energy and appears to be approaching an asymptote with increasing chain length, similar to the super-radiant mode, and as predicted by Willingham et al.,[28] although this plateau is not reached in the data shown in Figure 5. The spatial origin of the energy-loss signals at these peak energies for these peaks show a high loss probability predominantly at the central position within the oligomer with some also around the tips of the chains. For an even number of particles, the region of highest loss probability is located around the two central particles (see the image labeled L2 in Figure 3c), whereas for an odd number of particles the highest loss probability is around the central

dx.doi.org/10.1021/nl5009053 | Nano Lett. 2014, 14, 3799−3808

particle itself with some density extending around the adjacent particles for $N = 5$, as can be seen in Figure 4c L2. We observe these spatial areas are close to the central node for the dark subradiant ($l = 2$) mode, although without a significantly high loss density at the node position itself, obvious for even numbers of particles in the chain. These characteristics are consistent with EELS maps of hotspots (in the interparticle regions) of SERS-active structures with small interparticle separations[53] and the notion that the energy loss map is representative of the electric field for coupled systems.[49−52]

The $l = 3$ mode has a net dipole moment and is therefore a bright subradiant mode. We observe this mode for particle chain with $N = 3$ and $N = 5$ (Figures 2 and 4, respectively), although it is either absent or has too low loss probability to be observed for the $N = 4$ chain, either in the EELS experiments or modeled data. For the chain with $N = 3$, the individual dipole moments of each particle for the $l = 3$ mode are directly aligned along the interparticle axis with opposing oscillations, giving two nodes, each within the interparticle region (see Figure S1 of the Supporting Information). This highly repulsive mode has a loss peak with energy 2.3 eV. As the chain is extended to $N = 5$, the experimentally observed loss peak for this mode is observed as a broadening of the EEL spectra at around 1.8 eV. As this mode is able to be optically excited, we might expect it to be one of the main contributing resonances to the observed broadening of the super-radiant $l = 1$ mode observed in the scattering spectrum of the five particle chain.[2] This is in accord with the experimental results here. The mode makes a clear contribution to the modeled EEL spectra as the third lowest energy loss peak at 2.16 eV. The loss probability map at this energy is shown in Figure 4c L3. The evolution of the energies of the loss peaks for the $l = 3$ mode shift to lower energy with an increase in the number of particles in the chain.

Figure 5 shows the energy shift of the $l = 3$ mode with increasing chain length. Much like the $l = 2$ mode, the $l = 3$ mode originates in the trimer at an energy higher than the transverse mode. Although the energy for the $l = 3$ mode of the four particle chain is unknown, comparison between the energies of the $l = 3$ mode in the three and five particle chains highlights that the energy of this mode decreases with increasing chain length. It might be expected that this mode would energetically asymptote, in a similar fashion to the $l = 1$ and $l = 2$ modes and as reported theoretically.[28]

A few of the modes in the structures presented here proved difficult to detect with EELS. These modes are the $l = 2$, 3, and 4 modes for the three, four, and five particle chains, respectively, each of which take the form of $l = N - 1$. These modes become increasingly difficult to detect as N increases. This is because the $l = N - 1$ mode couples poorly to the incident electron beam and the energy of excitation increases with increasing N, meaning that it tends to be shielded by the transverse and higher order modes within the chain. It can therefore be said that modes where $l < N$ are more easily differentiated via EELS, whereas modes where l approaches N become increasingly difficult experimentally resolve.

As the chain length increases and the energies of the modes tend toward the energy of the super-radiant mode,[28] differentiation between and assignment of additional higher energy modes becomes increasingly difficult. The experimental and modeled data support the firm assignment of only one $l = 4$ mode (for the $N = 4$ chain) and one $l = 5$ mode (for the $N = 5$ chain). Notably, these modes both contain one complete charge oscillation per particle in the chain with nodes thus in-between every particle in the chain. The $l = 4$ mode is a dark subradiant mode, while the $l = 5$ mode is a bright subradiant mode. The loss peaks for these are at an energy of 2.3 eV experimentally, however, they are significantly broadened and more obvious in the modeled data at approximately 2.5 eV. The highest energy mode observed for each of the structures with $N = 2$ to $N = 5$ thus moves between being dark for even numbers of particles in the chain and bright for odd numbers. The modes are all highly repulsive due to the closeness of like charges in the area of closest approach between each particle in the chain with an energy relatively invariant across the series at 2.3−2.4 eV (experimental, 2.5 eV modeled). The electron energy loss peaks of these modes are present in the spectrum only when the high energy electrons are focused in the small gaps between the particles in the chain. The energy loss probability maps show the areas of highest loss probability are immediately surrounding each particle for every chain. The presence of higher order modes or quadrupole modes at around the energies of these modes cannot be excluded and there may be some contribution to the loss peaks at 2.3−2.4 eV from these.

Conclusions. In conclusion, the plasmonic properties of gold nanosphere chains from 1 to 5 particles in length have been investigated via EELS and compared with BEM modeling. We have demonstrated the existence of $l = 1$, 2, 3, 4, and 5 modes in nanochains up to five particles in length through the use of EELS point spectra and EELS mapping of individual modes. The evolution of subradiant modes within nanoparticle chains can be summarized as follows: a chain containing N nanoparticles can support $l = N$ of experimentally observable radiant modes and a transverse mode. The energy of the antibonding transverse mode is relatively invariant across the structures. The $l = N$ mode appears in the chain spectrum at an energy higher than the transverse mode (2.4 eV for the chains shown here). The addition of another nanoparticle onto the chain causes modes $l = 1, 2...N$ to decrease in energy, with a new $l = N + 1$ mode being supported by the chain with an energy of 2.4 eV. It was shown that modes where $l < N$ are relatively simple to detect and assign with difficulty increasing as l approaches N. As chain length increases further all $l = 1, 2...N$ modes energetically asymptote as they delocalize along the length of the chain forming a broadband resonance, linking the regimes of localized and traveling plasmons.

Methods. *Chemicals and Gold Nanosphere Preparation.* Gold(III) chloride trihydrate (99.9+%), and tris(2-carboxyethyl)phosphine hydrochloride (TCEP) were purchased from Sigma-Aldrich. All oligonucleotides were purchased from Geneworks. Cetyltrimethylammonium bromide (CTAB) was purchased from Ajax Chemicals. Spherical gold nanoparticles were prepared using the wet chemical synthesis developed by Rodriguez-Fernandez et al.[67] Briefly, citrate seeds were prepared by bringing 100 mL of aqueous 0.25 mM chloroauric acid ($HAuCl_4$) to boiling temperature. Seed growth is initiated by the addition of 3.5 mL of aqueous 1 wt % sodium citrate solution. A deep red color after 5 min of boiling indicates the presence of gold nanoparticle seeds. Growth solutions were then prepared by adding 1 mL of approximately 1 mM range concentration of aqueous $HAuCl_4$ to 88 mL of 0.015 M cetyltrimethylammonium bromide (CTAB). One milliliter of ascorbic acid is then added. The concentration of ascorbic acid was adjusted so that a 2:1 ratio of ascorbic acid to $HAuCl_4$ was present. Ten milliliters of seed solution was then

dx.doi.org/10.1021/nl5009053 | Nano Lett. 2014, 14, 3799−3808

added to initiate growth of the seeds followed by stirring for a few minutes. The concentration of $HAuCl_4$ needed was calculated from the volume of gold required to grow the 17 nm diameter seeds to the desired diameter.

Self-Assembly. The nanoparticles were assembled using thiolated single strand oligonucleotides via a method adapted from the work of Yao et al.[2,68] Thiolated oligonucleotide strands (purchased from Geneworks) were reduced with tris(2-carboxyethyl)phosphine hydrochloride (TCEP) and added to nanoparticle solutions to achieve a maximum DNA coverage. To form the oligonucleotide functionalized nanoparticles, 5 μL of an oligonucleotide solution (100 μM in oligomer concentration) was added to 45 μL of a 200 μM tris(2-carboxyethyl)phosphine hydrochloride (TCEP) solution. The resulting solution was left for 30 min to allow reduction of the terminal thiol moiety on the oligonucleotide. The reduced oligonucleotide solution was then added to 1000 μL of a solution of gold nanoparticles (generally 30−60 nm in diameter) and concentrations of approximately 6×10^{10} particles per milliliter. Equal volumes of nanoparticles functionalized with separate complementary DNA strands (e.g., S1 functionalized nanoparticles and S2 functionalized nanoparticles for the assembly of dimers and chains) were then mixed together, volumes of each sample of between 250 to 500 μL were used. Assembly reactions were then initiated by adding 3 mL of 0.1 M PBS buffer to the mixed nanoparticles. After the assembly reaction had proceeded for 1 min, the assembled particles were drop-coated onto plasma-cleaned carbon TEM grids. Once the sample had been allowed to sit for a minute, the TEM grid was dried under a stream of N_2, placed in a water bath at room temperature for 5 min, then removed and dried with a steady stream of N_2.

EELS Characterization. EELS signals were acquired from gold nanoparticles and nanoparticle chains using an FEI Titan 80-300 TEM equipped with a monochromator and a high-resolution spectrometer and operated at 80 keV. Particle imaging was performed in both parallel beam and scanning beam modes. In parallel beam mode, high-resolution images were acquired. Analysis of the particle optical properties, however, were performed in scanning beam mode, where the electron beam is focused to a point (approximately 2 nm in diameter) and scanned to form an image. In this mode, local EELS spectra can be recorded from a small excited volume by collecting low-angle scattered electrons and a dark-field image can be formed (simultaneously) by collecting high-angle scattered electrons with an annular detector. By raster scanning the beam, both structural and spectral information can be gathered from a rectangular region of interest in an approach termed spectrum imaging, forming a powerful means for rapid materials characterization at the nanometer level.[69]

Modeling. Finite element modeling was carried out using the Matlab based MNPBEM toolbox,[70] which solves Maxwell's equations for arbitrary geometries using the boundary element method.

■ ASSOCIATED CONTENT

Ⓢ Supporting Information

A schematic of the evolution of the plasmon modes in nanochains as a function of chain length; bright-field TEM images and normalized EELS spectra; line profiles of the experimental and calculated EELS maps; multipeak fit for spectrum 6 of the three particle chain; and calculated EELS intensity map, raw experimental EELS map, and experimental EELS map. This material is available free of charge via the Internet at http://pubs.acs.org.

■ AUTHOR INFORMATION

Corresponding Authors

*E-mail: (A.M.F.) alison.funston@monash.edu.
*E-mail: (G.A.B.) gbotton@mcmaster.ca.
*E-mail: (P.M.) mulvaney@unimelb.edu.au.

Notes

The authors declare no competing financial interest.

■ ACKNOWLEDGMENTS

S.J.B. thanks the University of Melbourne for a MATS scholarship and the Ernst and Grace Matthaei research scholarship. P.M. acknowledges Australian Research Council (ARC) support through LF 100100117. A.M.F. would like to thank the ARC for support via FT110100545 and DP120101573. G.A.B. is grateful to the Natural Sciences and Engineering Research Council (NSERC), Canada, for a Discovery grant supporting this work. The electron microscopy was carried at the Canadian Centre for Electron Microscopy, a national facility supported by NSERC and McMaster University.

■ REFERENCES

(1) Slaughter, L. S.; Willingham, B. A.; Chang, W.-S.; Chester, M. H.; Ogden, N.; Link, S. *Nano Lett.* **2012**, *12*, 3967−3972.
(2) Barrow, S. J.; Funston, A. M.; Gomez, D. E.; Davis, T. J.; Mulvaney, P. *Nano Lett.* **2011**, *11*, 4180−4187.
(3) Kneipp, K.; Kneipp, H.; Kneipp, J. *Acc. Chem. Res.* **2006**, *39*, 443−450.
(4) McFarland, A. D.; Van Duyne, R. P. *Nano Lett.* **2003**, *3*, 1057−1062.
(5) Rodriguez-Lorenzo, L.; Alvarez-Puebla, R. A.; Pastoriza-Santos, I.; Mazzucco, S.; Stephan, O.; Kociak, M.; Liz-Marzan, L. M.; Garcia de Abajo, F. J. *J. Am. Chem. Soc.* **2009**, *131*, 4616−4618.
(6) Eggeling, C.; Schaffer, J.; Seidel, C. A. M.; Korte, J.; Brehm, G.; Schneider, S.; Schrof, W. *J. Phys. Chem. A* **2001**, *105*, 3673−3679.
(7) Lim, D. K.; Jeon, K. S.; Kim, H. M.; Nam, J. M.; Suh, Y. D. *Nat. Mater.* **2010**, *9*, 60−67.
(8) Pillai, S.; Catchpole, K. R.; Trupke, T.; Green, M. A. *J. Appl. Phys.* **2007**, *101*, 093105−093105−8.
(9) Kowalska, E.; Mahaney, O. O. P.; Abe, R.; Ohtani, B. *Phys. Chem. Chem. Phys.* **2010**, *12*, 2344−2355.
(10) Reinhard, B. M.; Sheikholeslami, S.; Mastroianni, A.; Alivisatos, A. P.; Liphardt, J. *Proc. Natl. Acad. Sci. U.S.A.* **2007**, *104*, 2667−2672.
(11) Sonnichsen, C.; Reinhard, B. M.; Liphardt, J.; Alivisatos, A. P. *Nat. Biotechnol.* **2005**, *23*, 741−745.
(12) Mayer, K. M.; Lee, S.; Liao, H.; Rostro, B. C.; Fuentes, A.; Scully, P. T.; Nehl, C. L.; Hafner, J. H. *ACS Nano* **2008**, *2*, 687−692.
(13) Endo, T.; Kerman, K.; Nagatani, N.; Hiepa, H. M.; Kim, D. K.; Yonezawa, Y.; Nakano, K.; Tamiya, E. *Anal. Chem.* **2006**, *78*, 6465−6475.
(14) Yu, C. X.; Irudayaraj, J. *Anal. Chem.* **2007**, *79*, 572−579.
(15) Haes, A. J.; Van Duyne, R. P. *J. Am. Chem. Soc.* **2002**, *124*, 10596−10604.
(16) Maier, S. A.; Brongersma, M. L.; Kik, P. G.; Meltzer, S.; Requicha, A. A. G.; Atwater, H. A. *Adv. Mater.* **2001**, *13*, 1501−1505.
(17) Maier, S. A.; Kik, P. G.; Atwater, H. A. *Appl. Phys. Lett.* **2002**, *81*, 1714−1716.
(18) Shalaev, V. M. *Nat. Photonics* **2007**, *1*, 41−48.
(19) Alu, A.; Engheta, N. *Opt. Express* **2009**, *17*, 5723−5730.
(20) Alu, A.; Salandrino, A. *Opt. Express* **2006**, *14*, 1557−1567.
(21) Barrow, S. J.; Wei, X.; Baldauf, J. S.; Funston, A. M.; Mulvaney, P. *Nat. Commun.* **2012**, *3*, 1275.

(22) Quinten, M.; Leitner, A.; Krenn, J. R.; Aussenegg, F. R. *Opt. Lett.* **1998**, *23*, 1331−1333.
(23) Harris, N.; Arnold, M. D.; Blaber, M. G.; Ford, M. J. *J. Phys. Chem. C* **2009**, *113*, 2784−2791.
(24) Sweatlock, L. A.; Maier, S. A.; Atwater, H. A.; Penninkhof, J. J.; Polman, A. *Phys. Rev. B* **2005**, *71*, 7.
(25) Fung, K. H.; Chan, C. T. *Opt. Commun.* **2008**, *281*, 855−864.
(26) Funston, A. M.; Novo, C.; Davis, T. J.; Mulvaney, P. *Nano Lett.* **2009**, *9*, 1651−1658.
(27) Funston, A.; Davis, T. J.; Novo, C.; Mulvaney, P. *Philos. Trans. R. Soc. London, Ser. A* **2011**, *369*, 3472−3482.
(28) Willingham, B.; Link, S. *Opt. Express* **2011**, *19*, 6450−6461.
(29) Fujimoto, F.; Komaki, K.-i.; Ishida, K. *J. Phys. Soc. Jpn.* **1967**, *23*, 1186−1186.
(30) Fujimoto, F.; Komaki, K.-i. *J. Phys. Soc. Jpn.* **1968**, *25*, 1679−1687.
(31) Kreibig, U.; Zacharias, P. *Z. Phys.* **1970**, *231*, 128−143.
(32) Bosman, M.; Keast, V. J.; Watanabe, M.; Maaroof, A. I.; Cortie, M. B. *Nanotechnology* **2007**, *18*, 165505.
(33) Nelayah, J.; Kociak, M.; Stephan, O.; Garcia de Abajo, F. J.; Tence, M.; Henrard, L.; Taverna, D.; Pastoriza-Santos, I.; Liz-Marzan, L. M.; Colliex, C. *Nat. Phys.* **2007**, *3*, 348−353.
(34) Scholl, J. A.; Koh, A. L.; Dionne, J. A. *Nature* **2012**, *483*, 421−427.
(35) Yamamoto, N.; Ohtani, S.; Garcia de Abajo, F. J. *Nano Lett.* **2011**, *11*, 91−95.
(36) Chu, M.-W.; Myroshnychenko, V.; Chen, C. H.; Deng, J.-P.; Mou, C.-Y.; Garcia de Abajo, F. J. *Nano Lett.* **2008**, *9*, 399−404.
(37) Rossouw, D.; Couillard, M.; Vickery, J.; Kumacheva, E.; Botton, G. A. *Nano Lett.* **2011**, *11*, 1499−1504.
(38) Rossouw, D.; Botton, G. A. *Opt. Express* **2012**, *20*, 6968−6973.
(39) Rossouw, D.; Botton, G. A. *Phys. Rev. Lett.* **2013**, *110*, 066801.
(40) Koh, A. L.; Bao, K.; Khan, I.; Smith, W. E.; Kothleitner, G.; Nordlander, P.; Maier, S. A.; McComb, D. W. *ACS Nano* **2009**, *3*, 3015−3022.
(41) N'Gom, M.; Li, S.; Schatz, G.; Erni, R.; Agarwal, A.; Kotov, N.; Norris, T. B. *Phys. Rev. B* **2009**, *80*, 113411.
(42) Barrow, S. J.; Funston, A. M.; Wei, X.; Mulvaney, P. *Nano Today* **2013**, *8*, 138−167.
(43) Novo, C.; Funston, A. M.; Pastoriza-Santos, I.; Liz-Marzan, L. M.; Mulvaney, P. *Angew. Chem., Int. Ed.* **2007**, *46*, 3517−3520.
(44) Henry, A.-I.; Bingham, J. M.; Ringe, E.; Marks, L. D.; Schatz, G. C.; Van Duyne, R. P. *J. Phys. Chem. C* **2011**, *115*, 9291−9305.
(45) Nehl, C. L.; Grady, N. K.; Goodrich, G. P.; Tam, F.; Halas, N. J.; Hafner, J. H. *Nano Lett.* **2004**, *4*, 2355−2359.
(46) Billaud, P.; Marhaba, S.; Cottancin, E.; Arnaud, L.; Bachelier, G.; Bonnet, C.; Del Fatti, N.; Lerme, J.; Vallee, F.; Vialle, J. L.; Broyer, M.; Pellarin, M. *J. Phys. Chem. C* **2008**, *112*, 978−982.
(47) Ringe, E.; Langille, M. R.; Sohn, K.; Zhang, J.; Huang, J.; Mirkin, C. A.; Van Duyne, R. P.; Marks, L. D. *J. Phys. Chem. Lett.* **2012**, *3*, 1479−1483.
(48) Garcia de Abajo, F. J.; Kociak, M. *Phys. Rev. Lett.* **2008**, *100*, 106804.
(49) Bigelow, N. W.; Vaschillo, A.; Iberi, V.; Camden, J. P.; Masiello, D. J. *ACS Nano* **2012**, *6*, 7497−7504.
(50) Duan, H.; Fernandez-Dominguez, A. I.; Bosman, M.; Maier, S. A.; Yang, J. K. W. *Nano Lett.* **2012**, *12*, 1683−1689.
(51) Iberi, V.; Mirsaleh-Kohan, N.; Camden, J. P. *J. Phys. Chem. Lett.* **2012**, *4*, 1070−1078.
(52) Hohenester, U.; Ditlbacher, H.; Krenn, J. R. *Phys. Rev. Lett.* **2009**, *103*, 106801.
(53) Kadkhodazadeh, S.; Wagner, J.; Joseph, V.; Kneipp, J.; Kneipp, H.; Kneipp, K. *Plasmonics* **2013**, *8*, 763−767.
(54) Chu, M.-W.; Myroshnychenko, V.; Chen, C. H.; Deng, J.-P.; Mou, C.-Y.; Garcia de Abajo, F. J. *Nano Lett.* **2008**, *9*, 399−404.
(55) Okamoto, H.; Imura, K. *J. Mater. Chem.* **2006**, *16*, 3920−3928.
(56) Imura, K.; Okamoto, H.; Hossain, M. K.; Kitajima, M. *Nano Lett.* **2006**, *6*, 2173−2176.
(57) Huang, J.-S.; Kern, J.; Geisler, P.; Weinmann, P.; Kamp, M.; Forchel, A.; Biagioni, P.; Hecht, B. *Nano Lett.* **2010**, *10*, 2105−2110.
(58) Song, F.; Wang, T.; Wang, X.; Xu, C.; He, L.; Wan, J.; Van Haesendonck, C.; Ringer, S. P.; Han, M.; Liu, Z.; Wang, G. *Small* **2010**, *6*, 446−451.
(59) N 'Gom, M.; Ringnalda, J.; Mansfield, J. F.; Agarwal, A.; Kotov, N.; Zaluzec, N. J.; Norris, T. B. *Nano Lett.* **2008**, *8*, 3200−3204.
(60) Schaffer, B.; Hohenester, U.; Trugler, A.; Hofer, F. *Phys. Rev. B* **2009**, *79*, 041401.
(61) Stockli, T.; Bonard, J.-M.; Stadelmann, P.-A.; Chatelain, A. *Z. Phys. D: At., Mol. Clusters* **1997**, *40*, 425.
(62) Gunnarsson, L.; Rindzevicius, T.; Prikulis, J.; Kasemo, B.; Kall, M.; Zou, S. L.; Schatz, G. C. *J. Phys. Chem. B* **2005**, *109*, 1079−1087.
(63) Alu, A.; Engheta, N. *New J. Phys.* **2010**, *12*, 14 I..
(64) Ruting, F. *Phys. Rev. B* **2011**, *83*, 5.
(65) Chern, R.-L.; Chang, C. C.; Chang, C. C. *Phys. Rev. E* **2006**, *73*, 036605.
(66) Chern, R.-L.; Chang, C. C.; Chang, C. C. *Phys. Rev. B* **2006**, *74*, 155101.
(67) Rodriguez-Fernandez, J.; Perez-Juste, J.; de Abajo, F. J. G.; Liz-Marzan, L. M. *Langmuir* **2006**, *22*, 7007−7010.
(68) Yao, H.; Yi, C. Q.; Tzang, C. H.; Zhu, J. J.; Yang, M. S. *Nanotechnology* **2007**, *18*, 1−7.
(69) Maigne, A.; Twesten, R. D. *J. Electron. Microsc.* **2009**, *58*, 99−109.
(70) Hohenester, U.; Trugler, A. *Comput. Phys. Commun.* **2012**, *183*, 370−381.